



1 The 4-mode Modal Aerosol Module in C++ (MAM4xx) v1.0: 2 Representing Prognostic Aerosols in a Global Cloud-System 3 Resolving Atmosphere Model for GPU Exascale Computing

4 Jerome D. Fast¹, Balwinder Singh¹, Oscar Diaz-Ibarra², Jeff Johnson³, Chandru Dhandapani¹,
5 Brian Gaudet¹, Taufiq Hassan¹, Meng Huang¹, Jaelyn Litzinger¹, James Overfelt², Kyle Pressel¹,
6 Michael Schmidt², Shuaiqi Tang^{1,4}, Adam C. Varble¹, Hui Wan¹, Mingxuan Wu¹, Kai Zhang¹,
7 Po-Lun Ma¹.

8 ¹Pacific Northwest National Laboratory, Richland, Washington, United States

9 ²Sandia National Laboratory, New Mexico, United States

10 ³Cohere Consulting LLC, Seattle, Washington, United States

11 ⁴School of Atmospheric Sciences, Nanjing University, Nanjing, China

12

13 Corresponding author: Jerome D. Fast, jerome.fast@pnnl.gov

14

15 **Abstract.**

16 Aerosols are a key component of Earth system models since they affect meteorology and the Earth's
17 energy budget through complex cloud-aerosol-radiation interactions. Over the past decade, Earth system
18 models have increased their spatial resolution to better resolve atmospheric processes; however, this
19 advancement comes with significantly higher computational costs. To address this issue, some models
20 now take advantage of high-performance Graphics Processing Unit (GPU) exascale computer clusters
21 which offer faster processing capabilities with a higher level of parallelism than traditional Central
22 Processing Unit (CPU) systems, but these models still lack detailed representations of aerosols. In this
23 study, we describe the development of a new GPU-enabled prognostic aerosol model based on the four-
24 mode version of the Modal Aerosol Module (MAM4), called MAM4xx, that has been coupled to the
25 Energy Exascale Earth System (E3SM) Atmospheric Model (EAM) in C++ (EAMxx). To the best of our
26 knowledge, MAM4xx is the first fully GPU-enabled aerosol model with sophisticated process
27 representations. MAM4 has been completely rewritten in C++ using the Kokkos performance-portability
28 programming library while preserving all the physical and chemical processes in the original Fortran
29 version. The Kokkos library ensures compatibility across GPUs from various vendors and thus enables
30 execution on multiple GPU exascale high-performance computer clusters. We describe the steps
31 undertaken to port the code to C++/Kokkos as well as the rigorous testing methodology (i.e., unit tests,
32 real-world tests) so that the functionality remains intact and that bugs were not inadvertently introduced.
33 We demonstrate that MAM4xx coupled within EAMxx with ~12-km horizontal grid spacing behaves as
34 expected for real-world conditions based on comparison with observations and a reanalysis aerosol
35 dataset over the central U.S. during the spring of 2016. Currently, MAM4xx increases the computational
36 cost of the host atmospheric model by ~40%, which is due primarily to the treatment of aerosol-cloud
37 interactions, highlighting the need to optimize these processes for GPU computational efficiency. Future
38 improvements to MAM4xx will benefit from recent advancements in the physical representation of
39 aerosols in MAM4 as they are ported to C++/Kokkos. Additional testing for longer periods of time to
40 encompass a wider range of atmospheric conditions, over other geographic regions, and at higher spatial
41 resolution will be conducted in the future to more robustly assess simulated aerosol properties.



42 1 Introduction

43 Aerosol and aerosol-cloud interaction (ACI) processes remain the largest source of uncertainty in long-
44 term Earth system model predictions of global temperature (Forster et al. 2021; McCoy et al. 2020;
45 Bellouin et al. 2020). This uncertainty stems from complex, multi-scale processes that models struggle to
46 capture, such as how aerosols alter cloud micro- and macro-physical properties and how clouds alter
47 aerosol populations. These complex processes, in turn, influence the Earth’s radiation budget and water
48 cycle. Traditional global Earth system models are still fairly coarse, with horizontal grid spacings from
49 tens to a few hundred kilometers; therefore, part of the uncertainty in ACI likely arises to due to the
50 inability to adequately resolve cloud and aerosol populations as well as the intersection of clouds and
51 aerosols (e.g., Huang et al. 2025; Khain et al. 2025; Ma et al. 2014; Terai et al. 2020; Wang et al. 2025).
52 Consequently, models rely on parameterizations to represent these subgrid-scale processes that cannot be
53 resolved explicitly.

54 Several global convection permitting Earth system models have been developed over the past decade that
55 use horizontal grid spacings of a few to ten kilometers (i.e., kilometer-scale), similar to weather forecast
56 models. This includes models participating in the DYNAMICS of the Atmospheric general circulation
57 Modeled On Non-hydrostatic Domains (DYAMOND) model intercomparison (Stevens et al. 2019). This
58 spatial resolution permits the simulation of more realistic terrain and atmospheric conditions, particularly
59 for moist convection, though uncertainty still arises from the physics parameterizations approximating
60 many subgrid-scale processes. One example of a persistent bias in kilometer-scale Earth system models is
61 that too many precipitating convective cells are triggered that produce too much convective precipitation
62 and not enough stratiform precipitation (e.g., Caldwell et al. 2021; Su et al. 2026; Stanford et al. 2026;
63 Terai et al. 2025; Tian et al. 2024;). This bias is not alleviated at O(100-m) horizontal grid spacing (Zhang
64 et al. 2024), suggesting that inadequate subgrid-scale physics parameterizations are a primary source of
65 error instead of spatial resolution.

66 The Energy Exascale Earth System (E3SM) Atmospheric Model written in C++ (EAMxx) using the
67 Simple Cloud-Resolving E3SM Atmospheric Model (SCREAM) configuration (Caldwell et al., 2021) is
68 one of the new kilometer-scale global models that is designed to run on high-performance Graphical
69 Processing Unit (GPU) computer clusters (Donahue et al. 2024; Taylor et al. 2023). “xx” in the E3SM
70 community is used to denote C++ code to differentiate it from Fortran versions. The EAMxx code was
71 restructured into a data-parallel form using Kokkos (Trott et al. 2022) abstractions to achieve performance
72 portability across heterogeneous architectures (e.g., multi-core CPUs and GPUs from various vendors).
73 Donahue et al. (2024) assess the performance of four 40-day EAMxx simulations for each season ($\Delta x \sim$
74 3.25 km) using NASA satellite and Atmospheric Radiation Measurement (ARM, Stokes and Schwartz,
75 1994) data products. EAMxx has also been evaluated using a simulation of Hurricane Katrina’s evolution
76 (Bercos-Hickley et al., 2025), comparison of predicted spatiotemporal cloud variability with observations
77 and other global Earth system models (Chao et al., 2025), and examination of the effect of spatial
78 resolution on aerosol effective radiative forcing using prescribed aerosols (Mahfouz et al., 2025).

79 EAMxx currently uses prescribed aerosols for ACI and aerosol-radiation interaction (ARI) processes,
80 which are based on monthly 5-year climatologies of cloud condensation nuclei (CCN) and aerosol optical
81 properties with a spatial grid spacing of 1° generated by an E3SMv2 (Golaz et al., 2022) Atmospheric
82 Model Intercomparison Project (AMIP) configuration. The monthly values are then interpolated in time
83 and space for a particular simulation configuration. While this approach saves computational time by not
84 explicitly treating aerosols as prognostic variables, the magnitude and spatial variability of aerosol
85 properties will not be consistent with actual conditions. It is therefore desirable to have a prognostic
86 aerosol treatment option for EAMxx to better represent the aerosol lifecycle and consequently processes
87 affecting ACI and ARI that occur at kilometer-scale resolutions. The objectives of this study are to
88 describe 1) how the four-mode version of the Modal Aerosol Model (MAM4, Liu et al. 2016) was
89 completely rewritten in C++/Kokkos, 2) the testing procedure that ensures the new code represents the



90 same physical treatments as the Fortran version, and 3) the computational performance of the new code
91 called MAM4xx. In addition, a real-world case study is used to demonstrate that the new aerosol model
92 within EAMxx predicts spatiotemporal variations in aerosol mass, composition, size, and CCN
93 concentrations similar to observations and another global aerosol modeling system. As far as we know,
94 MAM4xx is the first fully GPU-enabled aerosol model with sophisticated treatment of aerosol processes
95 that can also run on multi-core CPU computer clusters. This paper serves as the documentation of the
96 model development and the first evaluation based on a case study.

97 **2 Model Description**

98 **2.1 EAMxx**

99 SCREAM (Caldwell et al. 2021) was designed to be a global convection permitting model using a grid
100 spacing of 3.25 km. While the original Fortran version of SCREAM (version 0) has been shown to
101 reproduce many aspects of observed cloud distributions, it is computationally expensive. To take
102 advantage of graphics processing units (GPUs) used by the world's fastest supercomputers and
103 significantly reduce the computational cost, the entire code was rewritten in C++/Kokkos. Kokkos (Trott
104 et al. 2022) enables C++ code to be compatible with GPUs from different manufacturers (e.g., AMD,
105 NVIDIA, SYCL), ensuring that the code can run on different GPU exascale supercomputers such as
106 Frontier operated by the Oak Ridge Leadership Computing Facility, Perlmutter operated by the National
107 Energy Research Scientific Computing Center (NERSC), and Aurora operated by the Argonne
108 Leadership Computer Facility (ALCF). The new E3SM Atmosphere Model in C++/Kokkos called
109 EAMxx is described in detail by Donohue et al. (2024). EAMxx was also awarded the Association for
110 Computer Machinery CM Gordon Bell special prize for climate modeling in 2023.

111 EAMxx uses the C++/Kokkos version of the Higher Order Method Modeling Environment (HOMME)
112 nonhydrostatic dynamical core. Physics parameterizations include the Rapid Radiation Transfer Model
113 for General circulation model applications - Parallel (RRTMGp, Pincus et al., 2019) parameterization to
114 represent radiation, the Simplified Higher Order Closure (SHOC, Bogenschutz and Kruger, 2013)
115 parameterization to represent cloud macrophysics and turbulence, and the Predicted Particle Properties
116 (P3, Morrison and Milbrandt, 2015) parameterization to represent cloud microphysics. Aerosols affect the
117 P3 cloud microphysics through cloud condensation nuclei (CCN) concentrations that are based on
118 monthly climatology and read into the model. This representation of cloud-aerosol interactions is referred
119 to as the Simple Prescribed Aerosols (SPA). The monthly climatology of SPA also includes aerosol
120 extinction and absorption that is used in RRTMG to account for aerosol-radiation effects. While the
121 computational cost of SPA is negligible, the climatological CCN and optical property distributions are
122 coarse in resolution (monthly 1°) and may or may not be consistent with simulated atmospheric
123 conditions. These Fortran codes were rewritten in C++/Kokkos and integrated into EAMxx. One
124 exception that has not been ported to C++/Kokkos is the E3SM Land Model (ELM) used to simulate the
125 exchanges between terrestrial land surface and other Earth system components. Instead, a coupler is used
126 to run ELM on CPUs while the rest of EAMxx runs on GPUs. The computational cost of ELM is
127 relatively small compared to other physics parameterizations; therefore, the coupling to CPUs for ELM
128 does not add a significant computational burden to the overall cost of EAMxx simulations.

129 As an alternative to the SPA treatment, a prognostic aerosol parameterization described next is integrated
130 into EAMxx to more realistically treat the aerosol lifecycle and consequently aerosol-cloud interactions
131 and aerosol-radiation interactions.

132 **2.2 MAM4**

133 The four-mode version of the Modal Aerosol Module (MAM4, Liu et al. 2016; Wang et al. 2020) is a
134 double-moment, 7-species representation of aerosols used by E3SM and the Community Earth System
135 Model (CESM, Mills et al. 2017; Tilmes et al. 2023), though the representations of some of the aerosol



136 processes in MAM4 in E3SM and CESM have diverged over time. MAM4 is similar to its precursor
137 MAM3 (Liu et al. 2012), except that MAM4 includes a primary carbon mode to represent the
138 microphysical aging of primary organic matter (POM) and black carbon (BC) in addition to simulating
139 the aerosol size distribution using Aitken, accumulation, and coarse modes. MAM4 includes
140 representations for prescribed primary emissions, online calculations of dust and sea-salt emissions,
141 nucleation, coagulation, secondary aerosol formation that includes sulfate (SO₄) and secondary organic
142 aerosol (SOA), dry deposition, wet scavenging, and aerosol-cloud-radiation interactions. As listed in
143 Table 1, MAM4 consists of 25 tracers representing aerosol mass composition and four tracers of aerosol
144 number for each mode. The Fortran version of the code is included in E3SM versions 1 - 3. The
145 performance of MAM4 within E3SM in representing aerosols and aerosol-cloud-radiation interactions is
146 well known and has been tested extensively (e.g., Christensen et al. 2023; Hasan et al. 2024; Liu et al.
147 2016; Tang et al. 2022, 2023; Shan et al. 2024; Varble et al. 2023; Wang et al. 2018, 2026; Wu et al.
148 2022).

149 2.3 GEOS-FP

150 Aerosol simulations made by the Goddard Earth Observing System Forward Processing modeling system
151 (GEOS-FP) are used in this study as a reference to assess the performance of MAM4xx predictions.
152 GEOS-FP is similar to GEOS Composition Forecast (GEOS-CF, Keller et al. 2021) in that meteorological
153 fields are based on the Modern-Era Retrospective analysis for Research and Applications Version 2
154 (MERRA-2, Gelaro et al. 2017) and aerosols are based on the Goddard Chemistry Aerosol Radiation and
155 Transport (GOCART, Chin et al. 2002) model. GOCART aerosols are constrained by satellite AOD
156 measurements from the Moderate Resolution Imaging Spectroradiometer (MODIS) from the Terra and
157 Aqua satellites (Randels et al. 2017; Buchard et al. 2017). GOCART is a single moment bulk aerosol
158 model that simulates aerosol mass. Aerosol number is not a predicted quantity but can be derived from
159 prescribed size distributions. Emissions are either calculated online (e.g., dust, sea-salt) or obtained from
160 the Hemispheric Transport of Air Pollution (HTAP) anthropogenic emission inventories. MODIS fire
161 radiative power measurements are also used to derive biomass burning emission rates as produced by the
162 Quick Fire Emissions Dataset (QFED, Darmenov and DaSilva, 2015).

163 Global GEOS-FP output was obtained for April and May 2016 and a subset of the output over the
164 continental U.S. is used to compare with MAM4xx and observations. Fifteen aerosol species are available
165 for black carbon, organic carbon (OC), sulfate, dust and sea salt (Table 1). It is important to note that
166 GEOS-FP treats organics as OC whereas MAM4xx treats organics as organic matter (OM). Aerosol
167 concentrations are available every 3 hours using a 0.3125° longitude by 0.25° latitude grid and 72 vertical
168 levels.

169 3 Code Development

170 The MAM4 version ported to C++/Kokkos originated from E3SMv2. The overall philosophy of porting
171 Fortran MAM4 to C++/Kokkos was to preserve the original functionality, enabling direct one-to-one
172 comparison between the Fortran and C++ implementations. In this way, differences in simulated aerosol
173 properties between E3SMv2 and EAMxx simulations would only be due to the differences in the other
174 physics parameterizations that will affect ambient meteorological conditions. For example, E3SMv2 uses
175 the Morrison and Gettleman (2008) treatment for cloud microphysics and the Cloud Layers Unified by
176 Binormals (CLUBB, Larson et al 2002) treatment for subgrid scale turbulence and cloud macrophysics,
177 while EAMxx uses P3 (Morrison and Milbrandt, 2015) and SHOC (Bogenschütz and Kruger, 2013).
178 Once MAM4xx is evaluated using real-world conditions to ensure the code was correctly reformulated in
179 C++/Kokkos, then additional improvements to aerosol treatments could be incorporated directly into
180 MAM4xx in the future.



181 Porting MAM4 to MAM4xx consisted of three steps, as shown in Fig. 1: 1) Fortran refactoring, 2) porting
 182 to C++, and 3) creating interfaces to integrate MAM4xx into EAMxx. As described in the next section,
 183 each step involved a series of tests to ensure that the resulting C++/Kokkos code has the same
 184 functionality as the original Fortran code. The Fortran codes were ported manually, since many of the
 185 tools for automated code conversion using artificial intelligence (AI) and large-language models (LLMs)
 186 had not yet been developed or were not mature at the time.

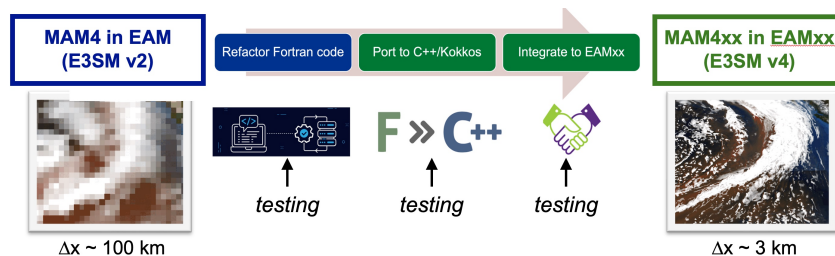


Figure 1: Diagram depicting the main steps used to port the MAM4 Fortran code to C++ and integrate it into the EAMxx model.

187 3.1 Step 1: Fortran Refactoring

188 The goal of refactoring the Fortran code was to restructure it so that it could be more easily and correctly
 189 ported to C++ and to enable rigorous testing of the port’s correctness. We started with a set of curated
 190 system-level regression tests that maximizes the code coverage of the MAM4 codes in E3SMv2. These
 191 tests included smoke, restart, and multi-node regression tests at various model resolutions and simulation
 192 lengths. Since these tests ran the full E3SMv2 model with real atmospheric conditions, they also captured
 193 the rare atmospheric events that are typically not seen in more idealized tests. Before refactoring,
 194 baselines were generated using these tests. During code refactoring, the generated baselines were
 195 compared against the refactored code to ensure bit-for-bit reproducibility for the entire refactor.

196 As the first step of refactoring, we removed all the “dead” MAM4 code that was not operational in
 197 E3SMv2. These codes were outdated and never tested under E3SMv2 (e.g., old MAM configurations
 198 such as MAM3 and MAM7, temporary research codes, and unused legacy codes from E3SMv1 and
 199 earlier code used in the Community Earth System Model, CESM). Our guiding principle for refactoring
 200 was modularization: we decomposed the large Fortran routines into smaller components to make the
 201 porting process more manageable and to facilitate systematic verification of each unit of code (i.e., unit
 202 testing). Each low-level routine was designed to perform a single, well-defined task, while higher-level
 203 driver routines invoked and coordinated these units to execute the overall workflow.

204 For testing the correctness of the port, we built a new Fortran-based testing infrastructure called
 205 FORTRESS (FORtran To C++ Record–rEplay teSt harnES) within E3SMv2. FORTRESS allows us to
 206 capture the inputs and outputs of all the refactored Fortran subroutines using simple code instrumentation.
 207 The captured inputs and outputs are stored in a YAML file format. A Python-based tool called
 208 SKYWALKER reads these YAML files to compare the outputs of Fortran routines against the ported
 209 C++ routines, given the same inputs (explained in section 3.2).

210 The FORTRESS design requires that Fortran subroutines use only intrinsic data types (e.g., int, real, char)
 211 with explicit argument intents (“in” for read only, “inout” for read and write, and “out” for write only).
 212 All derived-type arguments were eliminated and replaced with intrinsic types to simplify the Fortran



213 interfaces. This restructuring improved readability, made data flow explicit, and significantly simplified
214 rigorous testing and cross-language porting.

215 After the refactoring process, the new MAM4 code removed ~106,700 lines of Fortran code compared to
216 the original MAM4, substantially simplifying the overall implementation. The model results before and
217 after the refactor remained bit-for-bit identical due to our rigorous regression testing.

218 **3.2 Step 2: Porting code to C++/Kokkos**

219 After refactoring the Fortran MAM4 codes, the next step is to port individual small subroutines to
220 C++/Kokkos. To align with the EAMxx hierarchical parallelism, the loops that iterate over atmospheric
221 columns were stripped away. The loops that iterate over each level within a column were parallelized
222 using Kokkos parallelism constructs. The interior loops (e.g., loops over MAM4 species, modes, etc.)
223 were also parallelized wherever possible to exploit all parallelism offered by the MAM4 processes.

224 Since the subroutines were typically small and independent pieces, it was easy to divide the work among
225 developers. The input and output test data generated by FORTRESS infrastructure for each Fortran
226 subroutine were used here to test the correctness of each C++/Kokkos routine (i.e., validation testing). We
227 used the CTest utility to invoke these unit tests that run the C++ codes with the same input as the Fortran
228 codes. We expect the C++ routines to produce the same output as the Fortran routine. The SKYWALKER
229 tool was used to read the FORTRESS-generated input and compare C++ produced output with the
230 FORTRESS-generated output. Here, we did not expect to obtain the same bit-identical output between
231 C++ and Fortran codes since small differences would likely be produced by differences in compilers,
232 software environments, and the use of GPU hardware. Instead, if relative differences in the output from
233 Fortran and C++ codes were very small (i.e., attributable to numerical round-offs), then we considered the
234 code was ported correctly. If the differences were relatively large, the team would identify and fix any
235 bugs introduced to the code and execute the testing procedure again until the differences between the
236 Fortran and C++ code are at round-off levels.

237 To further test and debug the ported codes, we created a testing framework where synthetic data was
238 generated to invoke the C++ and Fortran routines. Since the data types were simple (integer, real,
239 character, etc.), it was straightforward to generate synthetic data and assemble it to invoke these routines.
240 For the same synthetic input, we expected the routines to produce the same output. This method helped us
241 catch many hard-to-find bugs and improved our code coverage. This also acted as an additional layer of
242 testing.

243 At this stage, variable names, shapes, sizes, and units were also changed to be consistent with EAMxx. In
244 this process, about 16,000 lines of C++ code were written to represent all aerosol physics and chemistry
245 in MAM4.

246 **3.3 Step 3: Integrate new code into EAMxx**

247 MAM4 (and hence MAM4xx) interacts with the host model at many different places in a time step for a
248 given process ordering. Each interaction requires a new interface code that translates and feeds EAMxx
249 inputs to MAM4xx codes and translates back the MAM4xx outputs to update EAMxx. This is unlike
250 other parameterization such as cloud microphysics (P3), macrophysics (SHOC), and radiation
251 (RRTMGP), which interact with the host model only once in a time step. We created seven new interfaces
252 to integrate all the MAM4xx processes into EAMxx. EAMxx configuration includes 10 processes, while
253 the EAMxx-MAM4xx configuration replaces SPA with MAM4xx to expand this to 16 processes. We had
254 the opportunity to combine a few of these interfaces into one to reduce the total number of interfaces. We
255 decided against it and added one interface for each MAM4xx process, as it provides us a clean way to test
256 each process in isolation and build unit tests at a more granular level.



257 Another challenge was the additional NetCDF files that MAM4xx needed to read, such as those for
258 primary emissions (surface and vertical) and online emissions (e.g., dust and sea salt) calculations, as well
259 as other calculations. EAMxx's SPA reads only one spatially and temporally varying NetCDF file, while
260 MAM4xx reads 21 files (e.g., information needed for dry deposition, oxidants, optical properties, dust
261 erodibility, and marine organics) with and without spatial and temporal variations. We extended
262 EAMxx's file reading capabilities to accommodate MAM4xx requirements.

263 Once each MAM4xx process passed the unit tests, we integrated them with EAMxx. Coarse resolution
264 simulations were conducted with the EAMxx model by turning on individual MAM4xx processes to
265 thoroughly test and analyze its output. Since we built the capability of turning on and off each MAM4xx
266 process individually, we could test each MAM4xx process coupled with EAMxx in isolation and reason
267 about its impact on a global model simulation. For example, sanity checks were performed when testing
268 the new emission code to ensure the highest aerosol concentrations were produced over the highest
269 emission regions, aerosol plumes were transported by the ambient meteorological conditions, and aerosol
270 burden continually increased. For aerosol microphysics, we examined when, where, and how much
271 secondary aerosols (SO₄, SOA) were produced, and that coagulation and condensation processes altered
272 the distribution of aerosols among the modes as expected. For aerosol optical properties, simulated AOD
273 from EAMxx was compared to equivalent E3SMv2 simulations, including checking that simulated
274 scattering and extinction altered the radiation budget as expected. Tests were also performed with and
275 without dry deposition to verify that aerosols were removed at the ground and that the total atmospheric
276 burden gradually decreased in the absence of other aerosol processes. Similarly, we verified that wet
277 scavenging was removed when and where hydrometeors were predicted by P3. Finally, simulated CCN
278 concentrations were assessed, and we examined cloud properties (e.g., droplet number) to determine
279 whether aerosol-cloud interaction processes, such as the Twomey effect, behaved as expected. While the
280 quantitative testing performed for steps 1 and 2 ensured that individual pieces of the code were ported
281 correctly, these qualitative tests revealed additional issues associated with the merging of MAM4xx code
282 with EAMxx so that they could be resolved.

283 After each aerosol process was tested individually, aerosol processes were merged one at a time. Tests at
284 this stage sometimes produced unexpected behavior, revealing other issues that needed to be resolved.
285 After all the aerosol processes were integrated into EAMxx, coarse global simulations were performed
286 over long periods of time to ensure the code did not crash unexpectedly and produced reasonable
287 simulated aerosol fields. We found that the code often crashed, usually due to issues with rapidly
288 changing GPU cluster configurations and/or updates to the EAMxx code that also affected aerosol
289 processes in unexpected ways.

290 In this process, we added about 5,000 lines of new C++ code, to connect MAM4xx with the host model
291 EAMxx.

292 Some testing was conducted using a 3.5 km global grid, as in Donahue et al. (2024); however, the
293 computational cost limited simulation periods to a few days. Therefore, real-world testing of MAM4xx in
294 this study uses a 12-km global horizontal grid spacing.

295 **3.4 Computational Cost**

296 The overall computational expense of the various processes in EAMxx and MAM4xx is shown in Fig. 2,
297 based on a 10-day global simulation using a 12-km grid spacing. When the SPA treatment is used in
298 EAMxx to represent aerosols, the dynamical core uses most of the computation time (79%). In
299 comparison, physics makes up the remaining 21% of the time (Fig. 2a). The SPA treatment that
300 prescribes aerosols takes up 2% of the total computational burden. As shown in Fig. 2b, MAM4xx adds a
301 significant computational cost to EAMxx. While adding 25 scalars also adds computational cost to the
302 dynamical core via advection, MAM4xx alone comprises 40% of the total computational cost (Fig. 2b).



303 As shown in Fig. 2c most of that cost is due to the code associated with the aerosol-cloud interaction
 304 processes in MAM4xx. The objective of the creation of MAM4xx was to ensure that the code works as
 305 expected within EAMxx on GPU exascale clusters, but we did not consider optimizing the GPU kernels
 306 for computational efficiency at this time.

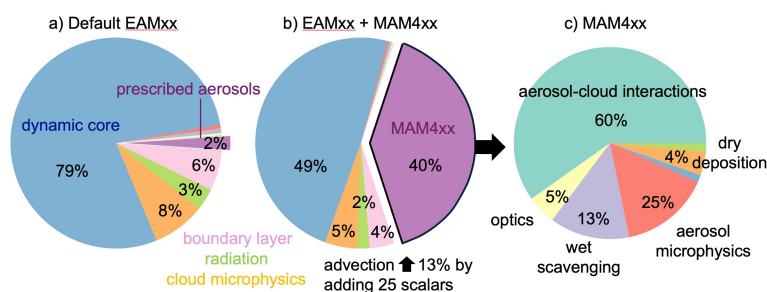


Figure 2: Relative computational cost for a) the default version of EAMxx, b) EAMxx with MAM4xx, and c) the cost of individual aerosol processes for a simulation on the Frontier supercomputer.

307 Part of the reason for the substantial computational expense is sub-cycling where ACI is invoked twice as
 308 often as other aerosol processes. In addition, we suspect that a large portion of the computational expense
 309 is due to the treatment of aerosol vertical mixing. In E3SMv2, a separate explicit-in-time vertical mixing
 310 treatment was included in MAM4, which was coupled with droplet activation within updrafts as part of
 311 the aerosol-cloud interaction modules. Thus, vertical mixing of aerosol scalars was not performed by the
 312 boundary layer parameterization as with other meteorological variables. This portion of MAM4 also
 313 required a large portion of the computational time in the Fortran version of the code. This treatment was
 314 preserved in EAMxx because our philosophy was to test the code processes as is. We expect that letting
 315 SHOC handle vertical mixing or adopting an implicit-in-time numerical scheme will result in significant
 316 cost savings; however, that would also require some modifications to the SHOC code or the current
 317 aerosol mixing parameterization.

318 The costs shown in Fig. 2 can be used in the future to target which pieces of the code can be reformulated
 319 to increase the efficiency on GPUs. We note that the relative computational cost of specific processes
 320 depends on the supercomputer. For example, we found that most of the computational expense of
 321 MAM4xx on Perlmutter was used by wet scavenging in contrast to the results shown for Frontier in Fig.
 322 2c.

323 4 Case Study Evaluation

324 4.1 Model Configuration

325 A 33-day global simulation of EAMxx from April 19 through May 21 2016 is used to demonstrate that
 326 the simulated aerosols from MAM4xx reasonably represent observations, focusing on measurements over
 327 the continental U.S. This spring period encompasses the first intensive observing period during the HI-
 328 SCALE field campaign (Fast et al. 2019) conducted around the ARM Southern Great Plains (SGP) site in
 329 north-central Oklahoma that has more detailed measurements of aerosol properties from operational
 330 surface monitoring networks, including aircraft measurements up to ~4 km MSL. The Earth System
 331 Model Aerosol-Cloud Diagnostics package (ESMAC Diags, Tang et al. 2022, 2023) developed for the
 332 Fortran version of E3SM, has been adapted to use EAMxx metadata and sub-1° resolution to compute
 333 some of the comparisons of observed and simulated aerosol quantities in this study.

334 The simulation uses a horizontal grid spacing of ~12 km and there are 128 vertical levels from the surface
 335 to the model top at 2.25 hPa. The initial conditions for winds, temperature, humidity, and ozone in



336 EAMxx were based on ECMWF reanalyses (ERA5, Hersbach et al. 2020). Horizontal winds are nudged
337 towards ERA5 at every vertical level using a nudging time scale of 6 hours. Aerosols are initialized from
338 an AMIP-style E3SMv2 simulation with 1° grid spacing. Anthropogenic emissions are obtained from
339 Community Earth atmospheric Data System (CEDS) released in 2021 that has 0.1° grid spacing. The
340 Global Fire Emissions Database (GFED, van der Werf, 2017) is used for biomass burning emissions that
341 vary from day to day based on satellite thermal anomalies. While there is a five-day spin up period prior
342 to the first HI-SCALE measurements on April 24, the aerosol distributions in the lower troposphere are
343 reasonably spun up within one simulation day.

344 EAMxx-MAM4xx simulations were conducted on the Department of Energy (DOE) Oak Ridge
345 Leadership Computing Facility's Frontier supercomputer using 192 GPU nodes and National Energy
346 Research Scientific Computing (NERSC) Perlmutter supercomputer using 256 GPU nodes, where each
347 node has 4 cores. On Perlmutter, the 33-day simulation took about 2.74 hours of wall-clock time to
348 complete, or about 0.82 simulated year per wall-clock day, compared to 0.71 simulated year per wall-
349 clock day on Frontier.

350 It is important to note that EAMxx was designed to be a global cloud-system scale resolving model,
351 targeting a horizontal grid spacing of ~3 km. As such, it does not have a parameterization to represent
352 cloud macrophysics as is commonly done in coarse global Earth system models. The treatment of sub-
353 grid scale clouds, transport, and precipitation in SHOC is not yet fully coupled with aerosols. Therefore,
354 the current EAMxx-MAM4xx simulation that uses a grid spacing of ~12 km will likely under-represent
355 the vertical mixing of aerosols due to convective transport and the removal of aerosols by wet scavenging.
356 It is not the objective of this paper to assess those uncertainties.

357 **4.2 Spatial and Temporal Variability in Aerosol Mass**

358 To illustrate the spatial variability of aerosol mass using a 12 km grid spacing, a snapshot of the predicted
359 surface PM_{2.5} concentrations from MAM4xx at 12 UTC (06 CST) on May 4, 2016, is shown in Fig. 3a.
360 Here, PM_{2.5} mass is defined as the sum of the Aitken and accumulation mode BC, organics, SO₄, dust,
361 and sea-salt. The large variations in aerosol mass over the south-central and southeastern U.S. are due to
362 the accumulation of anthropogenic emissions and secondary aerosols over urban areas within the shallow
363 nighttime stable boundary layer. Simulated PM_{2.5} from GEOS-FP at this time (Fig. 3b), defined as BC,
364 OC, SO₄, as well as dust and sea-salt from bin 1, is qualitatively similar to MAM4xx. For example, both
365 models produce northerly winds behind a cold front with lower aerosol concentrations that are advected
366 over eastern South Dakota, southern Minnesota, Iowa, and Wisconsin. Aerosol concentrations from both
367 models are also higher ahead of this cold front over the central U.S. However, aerosol concentrations
368 from GEOS-FP are lower behind the front and higher ahead of the front than those from MAM4xx,
369 resulting in a stronger horizontal gradient in aerosol mass. Animations of the simulated surface
370 concentrations (not shown) indicate that the driving synoptic meteorology that affects horizontal transport
371 is similar between the models; therefore, how each model represents aerosol physical processes and
372 emissions are likely driving the differences in concentrations. Another difference between the models is

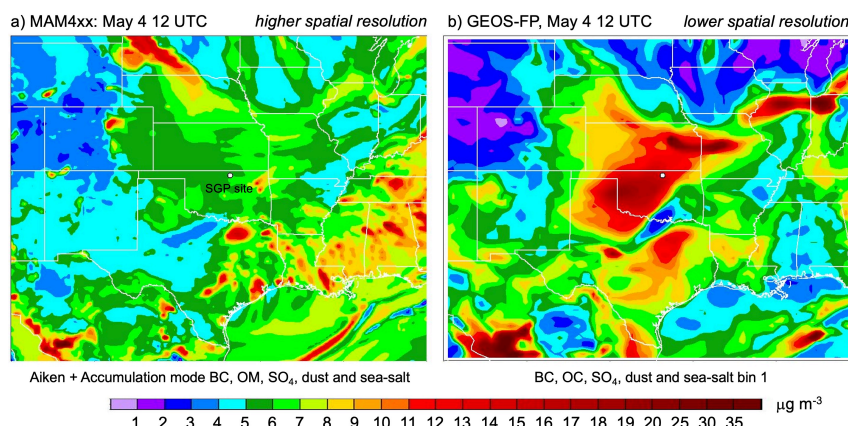


Figure 3: Fine mode aerosols simulated by a) MAM4xx and b) GEOS-FP at 12 UTC on May 4, 2016. The white dot denotes the location of the ARM SGP site where detailed surface and aircraft measurements of aerosol properties are available during the HI-SCALE field campaign period.

373 that the coarser spatial resolution of GEOS-FP does not produce distinct higher concentrations over urban
 374 areas as with MAM4xx.

375 A quantitative assessment of simulated PM_{2.5} at the Ponca City, Oklahoma EPA monitoring station is
 376 shown in Fig. 4. The average observed concentration during the simulation period (April 19 to May 22) is
 377 5.8 $\mu\text{g m}^{-3}$ and the bias in MAM4xx and GEOS-FP is -0.2 and 0.8 $\mu\text{g m}^{-3}$, respectively. Multi-day and
 378 diurnal variations in observed and MAM4xx concentrations are moderately correlated with a Pearson
 379 correlation coefficient (r) of 0.41. The correlation of observed and GEOS-FP concentrations over the
 380 same time period is somewhat higher ($r = 0.45$). In particular, GEOS-FP can represent spikes in PM_{2.5}
 381 (e.g., April 4 -5, 9, 13, 14) that are likely due to biomass burning plumes passing over the region since
 382 they are comprised mostly of organic carbon (not shown). Nevertheless, GEOS-FP does not reproduce all
 383 the PM_{2.5} spikes seen in the observations (e.g., April 22, May 14 and May 26) and sometimes simulates

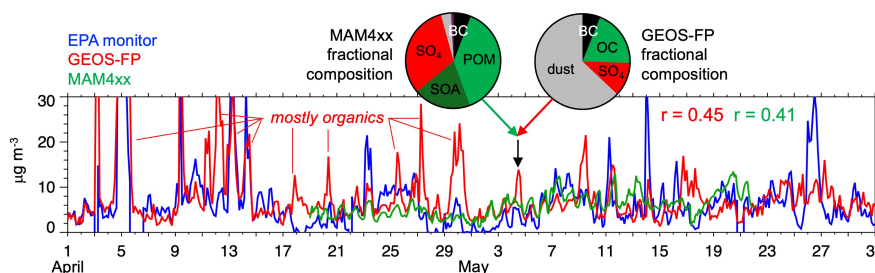


Figure 4: Time series of observed and simulated PM_{2.5} at Ponca City, Oklahoma (~30 km east of ARM SGP site). Pie charts denote fractional composition from both models at 12 UTC May 4, 2016, corresponding to the spatial distribution shown in Figure 3.

384 spikes that are not observed. The pie charts in Fig. 4 show the relative contribution of aerosol composition
 385 at 12 UTC, May 4, 2016, at the same time as Fig. 3. Aerosol mass from MAM4xx is comprised mostly of
 386 SO₄, primary organic matter (POM), and secondary organic aerosols (SOA). Previous Aerosol Chemical
 387 Speciation Monitor (ACSM) measurements in the region (Parworth et al., 2015) show that springtime
 388 OM is often the largest fraction of PM₁ concentrations over north-central Oklahoma and that primary
 389 organic aerosols, defined as hydrocarbon-like organic aerosol (HOA) via Positive Matrix Factorization



390 source apportionment, are a negligible fraction of fine mode organic matter. Therefore, the ratio of
 391 primary to secondary organic aerosols from MAM4xx is likely too high. The relative contribution of BC
 392 from both models is nearly the same. Conversely, GEOS-FP concentrations at this time are comprised
 393 mostly of dust which explains why aerosol concentrations are higher than MAM4xx over northern Texas,
 394 Oklahoma, Kansas, and Missouri (Fig. 3b). These results demonstrate that even when MAM4xx and
 395 GEOS-FP aerosol concentrations are similar, the simulated composition can be quite different.

396 Figure 5a is similar to Fig. 4, except that it represents an average of observed and simulated PM_{2.5} over
 397 all the EPA monitors within the domain shown in the lower right panel. The observed mass from all the
 398 EPA monitors is 7.84 $\mu\text{g m}^{-3}$. The simulated PM_{2.5} mass from GEOS-FP (7.63 $\mu\text{g m}^{-3}$) and MAM4xx
 399 (7.09 $\mu\text{g m}^{-3}$) is lower than observed. Both models represent the multi-day trends in aerosol mass over the

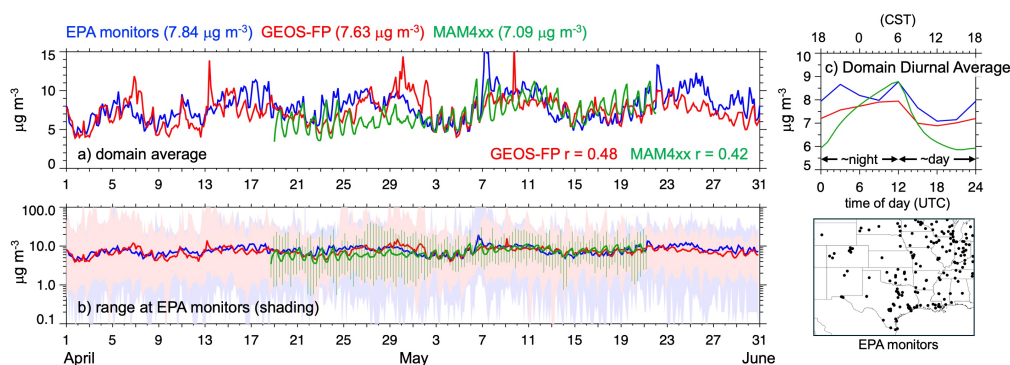


Figure 5: a) Average, b) range, and c) diurnal average of observed and simulated PM_{2.5} over central U.S. at stations as defined by the bottom right panel. Time of day expressed in UTC since stations encompass multiple time zones, although Central Standard Time (CST) denoted in c) to reflect night and day periods.

400 domain, with $r = 0.42$ and 0.48 for MAM4xx and GEOS-FP, respectively; however, the models struggle
 401 to represent the temporal trend in average aerosol mass during late April and early May. MAM4xx
 402 concentrations are too low between April 25 and May 1 and GEOS-FP concentrations are too high
 403 between April 29 and May 2. The range of PM_{2.5} concentrations simulated by MAM4xx at the EPA
 404 monitors (vertical green lines) is smaller than observed (light blue shading) as shown in Figure 5b. One
 405 reason for the inability of MAM4xx to represent peak aerosol concentrations is that it does not account
 406 for nitrate and ammonium; however, those two components are usually a small component of PM_{2.5}.
 407 More likely, the SOA treatment in MAM4xx is simple and likely under-represents the formation of SOA.
 408 The 12-km horizontal grid spacing also contributes to underestimates of clouds and rain which would act
 409 as a sink for aerosols. EAMxx currently does not have a sub-grid scale convection parameterization
 410 outside of SHOC so that wet scavenging may be too low which could explain why the model does not
 411 represent the lowest observed PM_{2.5} concentrations. The range of simulated PM_{2.5} from GEOS-FP (light
 412 red shading) is also smaller than observed, but it is closer to observations than MAM4xx.

413 Variation in emissions, boundary layer mixing, and secondary aerosol formation will result in diurnal
 414 variations in near-surface aerosol concentrations. Figure 5c shows the observed and simulated mean
 415 diurnal variations among all the EPA monitors. Not surprisingly, observations tend to be higher at night.
 416 While emissions are usually lowest during the night, the boundary layer is shallower so that vertical
 417 mixing and dilution is reduced compared to the daytime. Observed concentrations are lower during the
 418 day due to increased vertical mixing within the convective boundary layer that dilutes aerosol
 419 concentrations, despite condensational growth resulting from photochemical reactions. The diurnal
 420 variation from MAM4xx reproduces this overall trend; however, the diurnal variability is stronger than



421 observed which is also reflected in the time series shown in Fig. 5a. Conversely, GEOS-FP tends to have
 422 diurnal variations that more closely resemble observations, although the nighttime concentrations tend to
 423 be lower than observed.

424 A scatter plot of observed versus simulated PM_{2.5} is shown in Fig. 6a. Both models occupy the same
 425 footprint with MAM4xx having fewer stations with a positive bias (65 compared to 94) and more stations
 426 with a negative bias (126 compared to 97) than GEOS-FP. While the overall bias from both models is

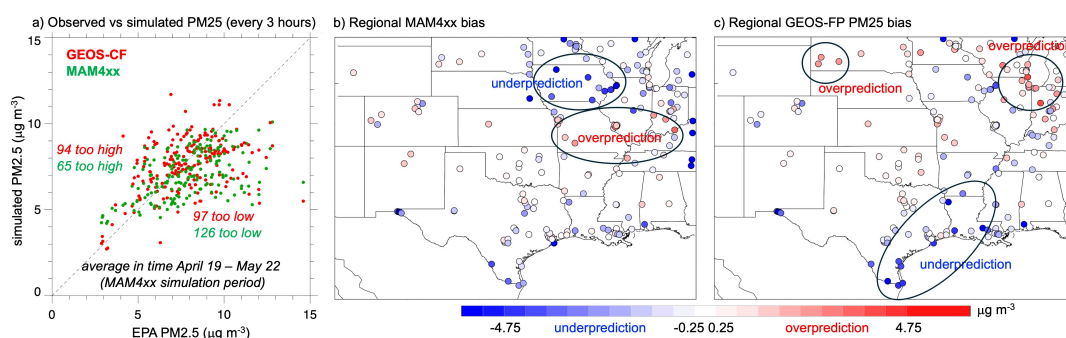


Figure 6: a) Errors in simulated PM_{2.5} and regional variations in overall bias from b) GEOS-FP and c) MAM4xx. Values in a) are every 3 hours at the same time intervals as the GEOS-FP analyses.

427 similar, there are differences in where the largest biases occur. In MAM4xx, the largest overpredictions
 428 are over the central Mississippi valley, and the largest underpredictions are over Iowa (Fig. 6b). In
 429 contrast, GEOS-FP tends to overpredict PM_{2.5} in the region surrounding Chicago and western South
 430 Dakota with underpredicted PM_{2.5} along the Gulf coast (Fig 6c).

431 The correlations of observed and simulated PM_{2.5} also show regional variations as shown in Fig. 7.
 432 MAM4xx has the highest correlations with $r > 0.5$ over most of southeastern Texas, while the lowest
 433 correlations close to zero are produced over the Midwest (Fig. 7a). The highest correlations with $r > 0.5$
 434 from GEOS-FP occur at stations over the central and northern Great Plains, while the lowest correlations
 435 near zero occur around Houston (Fig. 7b).

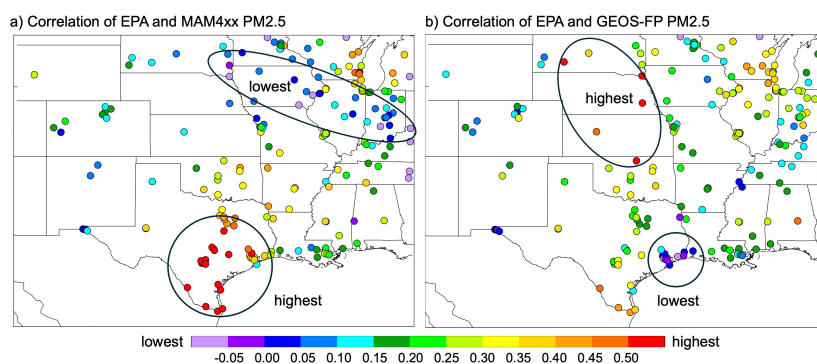


Figure 7: Regional variations in correlation between observed and simulated PM_{2.5} from a) GEOS-FP and b) MAM4xx.



436 **4.3 Aerosol Composition, Size, and CCN during HI-SCALE**

437 The ARM SGP site provides various measurements of aerosol properties that are useful to evaluate
 438 models. For example, the ACSM (e.g., Parworth et al. 2015) has obtained aerosol composition
 439 measurements of PM1 at this site for over a decade. The observed and simulated OM and SO₄ during
 440 April and May 2016, are shown in Fig. 8a. While the ACSM also measures NO₃, NH₄, and chloride, those
 441 species are not simulated by either model. The average total of OM and SO₄ between April 21 and May
 442 22 is 2.12 μg m⁻³. Both models have higher concentrations of 4.86 and 5.41 μg m⁻³ from MAM4xx and
 443 GEOS-FP respectively. The bottom two panels of Fig. 8a show this positive bias is mostly due to an

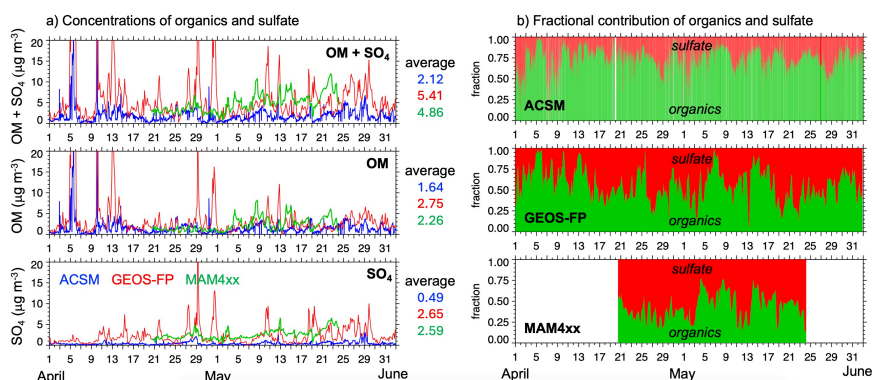


Figure 8: Observed and simulated a) surface concentrations and b) fractional contributions of organics and sulfate at the ARM SGP site in north-central Oklahoma.

444 overprediction in SO₄. MAM4xx produces a consistent bias throughout the simulation period, while
 445 GEOS-FP tends to produce intermittent SO₄ plumes that contribute to the overall bias. Both models are
 446 approximately five times higher than observed on average. In contrast, simulated OM is only about 1.4
 447 and 1.7 times higher than observed for MAM4xx, and GEOS-FP respectively. Figure 8b shows the
 448 observed and simulated relative fraction of OM and SO₄ as a function of time. While there are some
 449 periods where the ratio of OM and SO₄ is similar to observed, it is generally too low in both models.

450 There were also aircraft measurements of aerosol composition from an Aerosol Mass Spectrometer
 451 (AMS) as part of the HI-SCALE campaign. There were 17 flights where sampling was usually conducted
 452 within 100 km of the ARM SGP site up to an altitude of 4 km MSL. Most of the flights occurred between
 453 mid-morning and early afternoon. The ESMAC Diags package extracts MAM4xx simulation output at
 454 grid cells that most closely match the location and time along the aircraft flight paths. Figure 9
 455 summarizes the observed and simulated OM and SO₄ across all the flights with probability density
 456 functions (PDFs) using 0.2 μg m⁻³ bins. While the observed and simulated OM PDFs are similar between

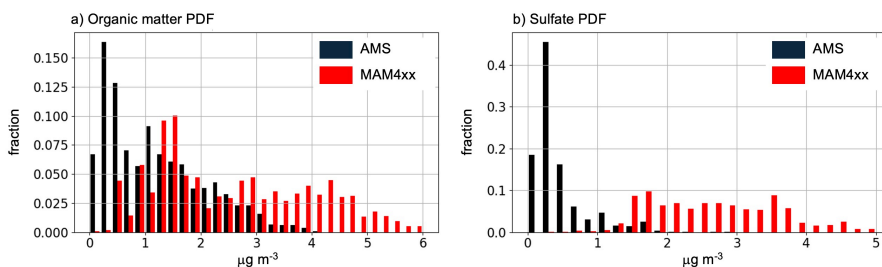


Figure 9: Observed and simulated probability density function of a) organic matter and b) sulfate for all G-laircraft flights during the HI-SCALE field campaign.



457 1 and $3 \mu\text{g m}^{-3}$, the model produces too many occurrences of higher OM concentrations between 4 and 6
 458 $\mu\text{g m}^{-3}$ that are not observed and too few occurrences of low OM concentrations $< 1 \mu\text{g m}^{-3}$ (Fig. 9a). In
 459 contrast, there is very little overlap in the observed and simulated PDFs of SO_4 (Fig. 9b) where MAM4xx
 460 usually produces concentrations greater than $1.5 \mu\text{g m}^{-3}$ while the observations are usually less than $1 \mu\text{g}$
 461 m^{-3} . These results are consistent with the biases at the surface as shown in Fig. 8, showing that
 462 overprediction of OM and SO_4 is not confined to the surface.

463 The Interagency Monitoring of Protected Visual Environments (IMPROVE) network also provides 3-day
 464 averages of aerosol composition measurements across the U.S. The simulated surface concentrations of
 465 BC, OM, SO_4 , and $\text{PM}_{2.5}$ from MAM4xx and GEOS-FP are averaged over the same 3-day periods and
 466 compared with the IMPROVE network measurements that are available during the simulation period (Fig.
 467 10). The locations of the IMPROVE monitors are shown in the right panel of Fig. 10. The locations of the

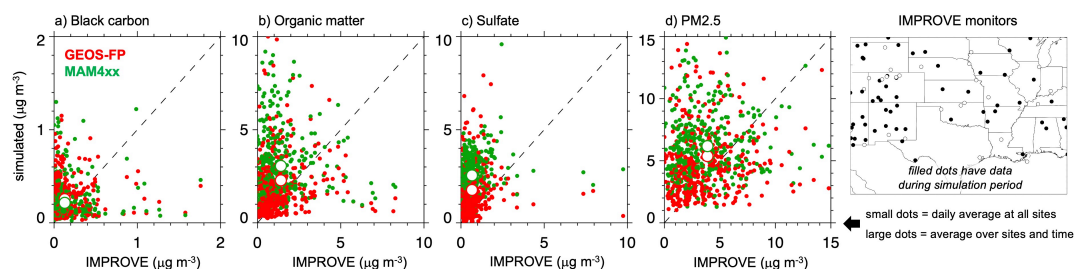


Figure 10: Scatter plots of observed and simulated a) black carbon, b) organic matter, c) sulfate, and d) $\text{PM}_{2.5}$ at IMPROVE monitoring stations over the central U.S.

468 IMPROVE monitors are shown in the right panel of Fig. 10. While there are often large errors in
 469 simulated BC for some sites and periods, simulated BC averaged over all the sites between April 19 and
 470 May 22 is similar to observed (Fig. 10a). As with the SGP site, both models tend to have OM and SO_4
 471 that is higher than observed (Figs 10b and 10c), with average OM concentrations closer to observed than
 472 SO_4 . While average simulated $\text{PM}_{2.5}$ concentrations at the EPA monitors is somewhat lower than
 473 observed (Fig. 4), average simulated $\text{PM}_{2.5}$ at the IMPROVE sites (Fig. 10d) is somewhat higher than
 474 observed. This difference is likely due to measurement site locations. IMPROVE sites are in rural regions
 475 and western U.S., while EPA monitors tend to be located within or close to cities in the eastern U.S.

476 There were also several instruments (FIMS, UHSAS, PCASP, CAS, FCDP) that measured portions of the
 477 aerosol size distribution on the aircraft. These measurements have been merged into a single product,
 478 called the Best Estimate Aerosol Size Distribution (BEASD), that used here to compare with the
 479 MAM4xx simulated size distribution. As with the aircraft aerosol composition (Fig. 9), the aerosol size
 480 distribution is extracted from the model output along the flight paths in ESMAC Diags. The average and
 481 range of values of aerosol number as a function of aerosol diameter are shown in Fig. 11. While simulated
 482 aerosol number concentrations are similar to observations between 150 and 400 nm diameters, they are
 483 usually lower than observed for diameters less than 100 nm higher than observed for diameters between
 484 400 and 1000 nm. The simulated aerosol number concentration variability is also less than observed,
 485 consistent with predictions of $\text{PM}_{2.5}$ (Fig. 4). The overprediction in aerosol number between 400 and
 486 1000 nm is consistent with the high bias in OM and SO_4 shown in Fig. 9. The underprediction in aerosol
 487 number for diameters less than 150 nm is likely due to the simple aerosol nucleation scheme that
 488 represents new particle formation (NPF) and using only the Aitken mode to represent the smallest
 489 particles. Zhao et al. (2024) added 11 NPF mechanisms and an ultrafine mode in E3SMv1 to better
 490 represent nucleation and particle growth to larger sizes and showed improvements in the simulated
 491 aerosol size distribution. These mechanisms are not incorporated into MAM4xx; therefore, porting this



492 code to C++ and integrating it with MAM4xx in the future will likely improve the representation of the
 493 aerosol size distribution.

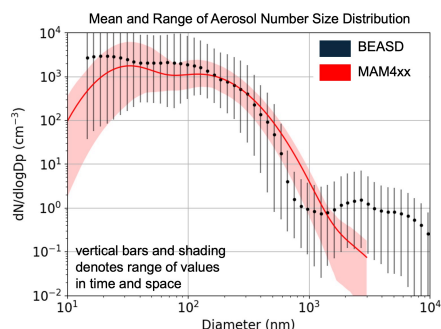


Figure 11: Observed and simulated aerosol number size distribution for all G-1aircraft flights during the HI-SCALE field campaign. Black dots and red line are mean values. Vertical bars and shading denote the 5th to 95th percentiles along the flight paths that vary in space and time.

494 Aerosol composition (via hygroscopicity), aerosol size distribution, and supersaturation over liquid water
 495 are factors that determine cloud condensation nuclei (CCN) concentrations (e.g., Abdul-Razzak and
 496 Ghan, 2000; Petters and Kreidenweis et al. 2007; Twomey, 1974) that influence cloud droplet activation
 497 and cloud properties. Figure 12 shows the observed and simulated CCN concentration PDFs along the HI-
 498 SCALE aircraft flight using 50 cm⁻³ bins. The observed and simulated PDFs overlap for both 0.2 and
 499 0.5% supersaturations, although MAM4xx produces a narrower distribution that does not produce as
 500 many low and high CCN concentrations as observed. Given the high bias in OM and SO₄ concentrations
 501 (Fig. 9) and the high biased SO₄ to OM ratios that will lead to higher than observed hygroscopicity, it
 502 may be surprising that CCN concentrations are not biased high as well. Since aerosol number
 503 concentrations between 100 and 300 nm are reasonably simulated on average, errors in aerosol size
 504 distribution may not have as large of effect on CCN at 0.2% supersaturation. At higher supersaturations
 505 such as 0.5%, smaller aerosols with diameter down to 25 nm can activate. Nevertheless, errors in
 506 simulated CCN at 0.5% are similar to those at 0.2% even though the model underestimates aerosol
 507 concentrations smaller than 150 nm. The specific factors contributing to CCN errors are likely due in part
 508 to compensating errors; however, understanding these compensating errors would require a CCN closure
 509 study that is beyond the scope of this paper.

510

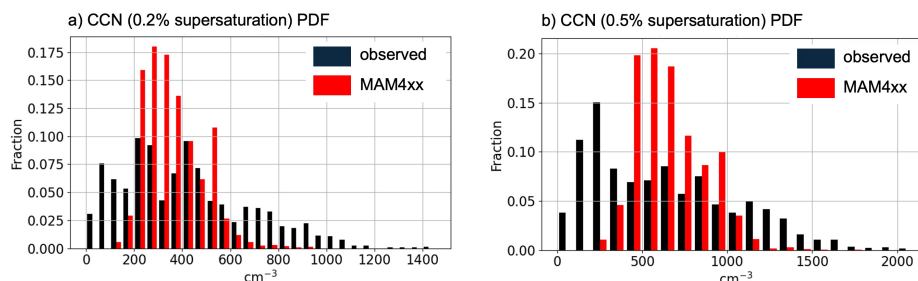


Figure 12: Observed and simulated CCN at a) 0.2% and b) 0.5% supersaturation for all G-1aircraft flights during the HI-SCALE field campaign.

511 **4.4 Aerosol Optical Depth**



512 Aerosol optical depth (AOD) is used to evaluate the performance of simulated aerosols throughout the
 513 atmospheric column. The optical properties of aerosols influence the radiation budget via scattering and
 514 absorption. The ARM SGP central facility (E13) provides measurements of AOD at 500 nm derived from
 515 an MFRSR instrument (Fig. 13). Data are not available during the night or during cloudy periods. There
 516 are also two other sites within 80 km of the central facility that also provide AOD measurements, E39 and
 517 E40, that are used to show variability of AOD. Simulated AOD for the MAM4xx grid cell that
 518 encompasses the E13 site are usually higher than observed. The average observed AOD during the period
 519 is 0.063 while the average AOD from MAM4xx is 0.149, about 2.4 times higher than observed. This is
 520 consistent with the high bias in OM and SO₄ at both the surface (Fig. 8a) and aloft (Fig. 9). The vertical
 521 lines denote the simulated range of AOD for all MAM4xx grid cells within 80 km of the SGP central
 522 facility. However, additional AOD measurements are needed to better characterize the observed spatial
 523 variability that could be used to evaluate the simulated spatial variability.

524 We also compared the simulated AOD averaged over the simulation period with those from the MODIS

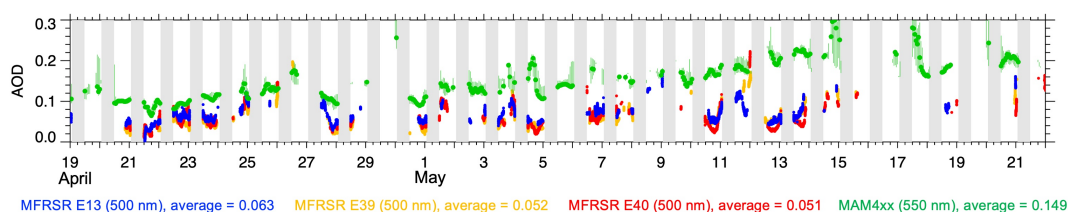


Figure 13: Observed and simulated AOD at the ARM SGP site. E13, E39, and E40 are three sites around the SGP site where AOD at 500 nm is obtained from the MFRSR instrument. Vertical lines denote range of MAM4xx AOD up to 80 km from E13. Gray shading denotes nighttime periods.

525 Aqua satellite (Fig. 14). The white areas in Fig. 14a are missing data and the dots in Figs. 14a and 14b
 526 represent average AOD from NASA’s Aerosol Robotic Network (AERONET) sites. The missing data
 527 from MODIS is most likely due to cloud cover in certain regions during the overpass times. In contrast,
 528 EAMxx produces fewer clouds at these overpass times, and thus Fig. 14b indicates that there is simulated

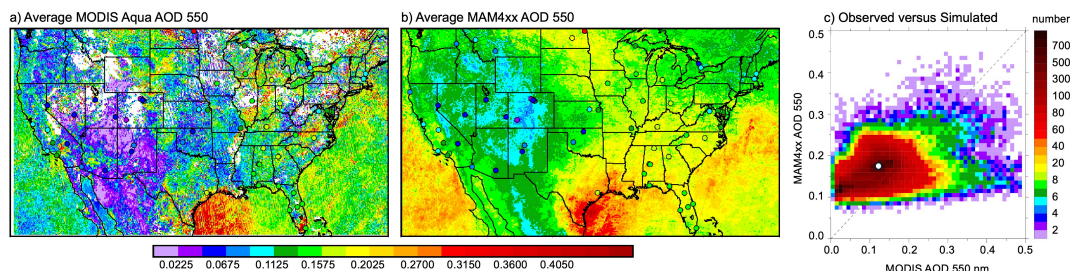


Figure 14: Spatial distribution of average AOD at 550 nm during the simulation period from a) MODIS Aqua b) MAM4xx at the approximate time of the MODIS Aqua overpass. c) Heat map depicting observed versus simulated AOD averaged over the domain at each MAM4xx grid cell. Dots in a) and b) denote averages from AERONET monitors.

529 clear-sky AOD for each grid cell on at least one of the simulation days.

530 Not surprisingly, the AERONET and MODIS data are usually consistent (Fig. 14a). The simulated spatial
 531 pattern in AOD is similar in some respects to MODIS. The highest AOD is observed and simulated over
 532 the western Gulf of Mexico and the lowest AOD is observed and simulated over the interior of the
 533 western U.S. and western Mexico. While the simulated AOD from MAM4xx is usually too high, there are
 534 regions in the Midwest and northeastern U.S. where the simulated AOD is too low. Figure 14c directly



535 compares the average AOD from MAM4xx over the simulation period at each grid cell compared with
536 the equivalent values from MODIS AOD for the same grid cells. The white dot in Fig. 14c denotes
537 average values from MODIS and MAM4xx which are 0.127 and 0.165, respectively. Figure 14c also
538 shows that the minimum AOD from MAM4xx is rarely less than 0.09, even though such values are
539 common in observations. Thus, while MAM4xx reproduces the overall geographical pattern of AOD,
540 values are more commonly too high than too low, with substantial regional variability in biases.

541 **4 Summary and Future Directions**

542 The development of a new GPU-enabled aerosol model called MAM4xx has been described that also runs
543 on multi-core CPU computer clusters. While the underlying physics is the same as in the MAM4 model
544 written in Fortran, the code was been completely rewritten in C++/Kokkos. The overall process of porting
545 MAM4 to C++/Kokkos was done in three steps: 1) refactoring the Fortran code, 2) manually porting the
546 code to C++/Kokkos, and 3) integrating the code into the E3SM code base. Each step consisted of series
547 of rigorous tests to ensure the functionality did not change and that bugs were not introduced. This
548 included unit-testing where small pieces of new code are run with a range of input values to ensure the
549 output values are identical or nearly identical to those obtained from the original code. It also included
550 simulations of individual aerosol processes using a coarse global model configuration to ensure consistent
551 values for real-world conditions.

552 We further demonstrated that MAM4xx coupled within EAMxx behaves as expected by simulating a
553 previously documented ~1-month case study over the central U.S. during the spring of 2016 using 12-km
554 horizontal grid spacing covering the globe. Performance is assessed by comparing predictions of aerosol
555 properties with observations and the GEOS-FP global aerosol model. GEOS-FP can be considered a
556 global aerosol reanalysis product, since aerosols are constrained by satellite measurements of AOD. We
557 demonstrate that simulated aerosol mass, composition, and size compare reasonably well with surface and
558 aircraft observations. While there are many differences in the configuration of EAMxx-MAM4xx and
559 GEOS-FP, simulated aerosol mass and composition is also shown to be similar in many respects. While
560 MAM4xx exhibits biases in some simulated aerosol properties, those biases are consistent with the
561 original MAM4 model coupled with E3SMv2.

562 The MAM4xx computational performance on a GPU cluster was quantified, showing that the updated
563 version of EAMxx requires ~40% of its time on aerosol processes. However, most of the additional
564 computational burden is due to aerosol-cloud interaction processes. Since this computational expense is
565 isolated in one process module, developing alternative code that is more efficient on GPUs should be
566 possible.

567 Now that we have demonstrated that MAM4xx coupled with EAMxx functions as expected, additional
568 improvements can now be considered. First, this and other previous evaluation studies show that
569 increasing spatial resolution improves spatiotemporal variability but does not eliminate biases; thus, the
570 treatment of physical processes within parameterizations still require improvement. This includes
571 processes contributing to the overpredictions of SO₄ and the ratio of primary to secondary organic
572 aerosol. MAM4xx could also take advantage of improved process representations developed for the
573 Fortran version of MAM4 over the past few years, such as the new particle formation mechanisms and
574 ultrafine mode (Zhao et al., 2024), improved Dimethyl Sulfide (DMS) chemistry (Kang et al., 2025),
575 incorporation of agricultural dust (Shi et al., 2025) and wildfire aerosol plumes (Lu et al., 2023), neural
576 network-based aerosol optics (Geiss and Ma, 2025) improved aerosol activation (Silva et al., 2021), and
577 modifications to MAM4 within E3SM version 3 (Wang et al. 2026). These treatments in Fortran would
578 need to be ported to C++/Kokkos and tested within EAMxx. Second, it would be useful to couple
579 MAM4xx with the C++/Kokkos version of the doubly periodic configuration of SCREAM, called DP-
580 SCREAM (Bogenschulz et al. 2023). DP-SCREAM is a limited area version of SCREAM, which is better



581 suited to developing and testing new treatments since the computational expense is significantly lower.
582 Third, MAM4xx should also be evaluated within EAMxx at higher resolution using the global 3-km grid
583 configuration. It is likely that some of the treatments in MAM4xx, particularly those associated with
584 aerosol-cloud interactions, will need to be reformulated to better suit kilometer-scale simulations. While
585 simulations longer than a season at convection-permitting scales are still computationally expensive on
586 GPU clusters, some evaluation could be done over shorter periods of time using a more diverse set of
587 observations that span tropical, mid-latitude, and Arctic regions including contrasting continental and
588 maritime regimes.

589 *Code availability.* The MAM4xx code is available at <http://github.com/eagles-project/mam4xx>, MAM4
590 Fortran code is available via the E3SMv2 repository at <http://github.com/E3SM-Project/E3SM>, and the
591 SKYWALKER python tool is available at <http://github.com/eagles-project/mam4xx>. The EAMxx with
592 MAM4xx code and the set-up script used for the simulations used in this study have been archived at
593 <https://doi.org/10.5281/zenodo.19140449> (Fast et al. 2026).

594 *Data availability.* Global GEOS-FP output was obtained from a NASA archive and available at
595 <https://portal.nccs.nasa.gov/datashare/gmao/geos-fp/das>. ARM in situ and remote sensing observations
596 are publicly available at <https://adc.arm.gov/discovery/#/>. Air quality monitoring data from EPA and
597 IMPROVE was obtained from https://aq5.epa.gov/aq5web/airdata/download_files.html and
598 <https://vista.cira.colostate.edu/Improve/>, respectively. AOD from MODIS satellite and AERONET
599 ground sites were from <https://ladsweb.modaps.eosdis.nasa.gov/search/>, and
600 https://aeronet.gsfc.nasa.gov/new_web/webtool_aod_v3.html, respectively.

601 *Author contributions.* J.F. lead the code conversion effort, performed the evaluation shown in Section 3,
602 and wrote the manuscript. B.S. and O.D.-I. were task leads for the code conversion effort consisting of
603 J.J., C.D., B.G., M.W., J.L., J.O. K.P., M.S., S.T., H.W., M.W., and KZ. The EAMxx simulation was
604 performed by P.-L.M., T.H. provided emissions, A.V. ran the ESMACS diagnostics. All investigators
605 contributed to editing the manuscript.

606 *Competing interests.* Po-Lun Ma is a member of the editorial board of Geoscientific Model Development.
607 All other authors have declared no competing interests.

608 *Disclaimer.* Publisher's note: Copernicus Publications remains neutral with regard to jurisdictional claims
609 made in the text, published maps, institutional affiliations, or any other geographical representation in this
610 paper. While Copernicus Publications makes every effort to include appropriate place names, the final
611 responsibility lies with the authors. Views expressed in the text are those of the authors and do not
612 necessarily reflect the views of the publisher.

613 *Acknowledgements.* This research used resources of the Oak Ridge Leadership Computing Facility at the
614 Oak Ridge National Laboratory, which is supported by the Office of Science of the U.S. Department of
615 Energy under Contract No. DE-AC05-00OR22725. This research also used resources of the National
616 Energy Research Science Computing Center (NERSC), a U.S. Department of Energy Office of Science
617 User Facility located at Lawrence Berkley National Laboratory, operated under contract DE-AC02-
618 05CH11231, using NERSC awards BER-ERCAP0033555 and BER-ERCAP0037401. The GEOS-FP
619 data used in this study/project have been provided by the Global Modeling and Assimilation Office
620 (GMAO) at NASA Goddard Space Flight Center. We thank the E3SM team for providing technical
621 expertise needed to couple MAM4xx with EAMxx and the Global Modeling and Assimilation Office
622 (GMAO) at the NASA Goddard Space Flight Center for providing the GEOS-FP data used in this study.
623 IMPROVE is a collaborative association of state, tribal, and federal agencies, and international partners.
624 US Environmental Protection Agency is the primary funding source for IMPROVE, with contracting and
625 research support from the National Park Service. The Air Quality Research Center at the University of



626 California, Davis is the central analytical laboratory, with ion analysis provided by Research Triangle
627 Institute, and carbon analysis provided by Desert Research Institute. We thank the numerous AERONET
628 PIs and their staff for establishing and maintaining the sites used in this investigation.

629 *Financial support.* This effort was supported as part of the “Enabling Aerosol-cloud interactions at
630 GLobal convection-permitting scales (EAGLES)” project (project no. 74358), sponsored by the U.S.
631 Department of Energy, Office of Science, Office of Biological and Environmental Research, Earth
632 System Model Development (ESMD) and Regional and Global Model Analysis (RGMA) program areas.
633 The Pacific Northwest National Laboratory (PNNL) is operated for the DOE by the Battelle Memorial
634 Institute under contract DE-AC06-76RL01830.



635 References

- 636 Abdul-Razzak H., and Ghan, S.J.: A parameterization of aerosol activation 2. Multiple aerosol types. *J.*
637 *Geophys. Res.*, 105, 6837-6844, DOI:10.1029/1999JD901161, 2000.
- 638 Bellouin, N., Quaas, J., Gryspeerdt, E., Kinne, S., Stier, P., Watson-Parris, D., Boucher, O., Carslaw, K.
639 S., Christensen, M., Daniau, A. L., Dufresne, J. L., Feingold, G., Fiedler, S., Forster, P., Gettelman, A.,
640 Haywood, J. M., Lohmann, U., Malavelle, F., Mauritsen, T., McCoy, D. T., Myhre, G., Mülmenstädt, J.,
641 Neubauer, D., Possner, A., Rugenstein, M., Sato, Y., Schulz, M., Schwartz, S. E., Sourdeval, O.,
642 Storelvmo, T., Toll, V., Winker, D., and Stevens, B.: Bounding global aerosol radiative forcing of climate
643 change. *Rev. Geophys.*, 58, DOI:10.1029/2019rg000660, 2020.
- 644 Bercos-Hickey, E., Mahfouz, N., Keen, N.D., Patricola-DiRosario, C.M., Hannah, W.M., Beydoun, H.,
645 Wehner, M.F., Lin, W., Terai, C.R., and Hillman, B.: Simulating hurricane Katrina in the Simple Cloud-
646 Resolving E3SM Atmosphere Model v1. *J. Adv. Model. Earth Sys.*, 17(10), e2025MS005210, DOI:
647 10.1029/2025MS005210, 2025.
- 648 Bogenschutz, P.A., Eldred, C., and Caldwell, P.M.: Horizontal resolution sensitivity of the simple
649 convection-permitting E3SM atmosphere model in a doubly-periodic configuration. *J. Adv. Model. Earth*
650 *Sys.*, 15(7), e2022MS003466, DOI:10.1029/2022MS003466, 2023.
- 651 Bogenschutz, P.A., and Krueger, S.K.: A simplified PDF parameterization of subgrid-scale clouds and
652 turbulence for cloud-resolving models. *J. Adv. Model. Earth Sys.*, 5(2), 195-211.
653 DOI:10.1002/jame.20018, 2013.
- 654 Buchard, V., Randles, C.A., da Silva, A.M., Darnenov, A., Colarco, P.R., Govindaraju, R., Ferrare, R.,
655 Hair, J., Beyersdorf, A.J., Ziemba, L.D., and Yu, H.: The MERRA-2 aerosol reanalysis, 1980 onward.
656 Part II: Evaluation and case studies. *J. Climate*, 30(17), 6851-6872, DOI:10.1175/JCLI-D-16-0613.1,
657 2017.
- 658 Caldwell, P.M., Terai, C.R., Hillman, B., Keen, N.D., Bogenschutz, P., Lin, W., Beydoun, H., Taylor, M.,
659 Bertagna, L., Bradley, A.M., Clevenger, T.C., Donahue, A.S., Eldred, C., Foucar, J., Golaz, J.-C., Guba,
660 O., Jacob, R., Johnson, J., Krishna, J., Liu, W., Pressel, K., Salinger, A.G., Singh, B., Steyer, A., Ullrich,
661 P., Wu, D., Yuan, X., Shpund, J., Ma, H.-Y., and Zender, C.S.: Convection-permitting simulations with
662 the E3SM global atmosphere model. *J. Adv. Model. Earth Sys.*, 13, e2021MS002544.
663 DOI:10.1029/2021MS002544, 2021.
- 664 Chao, L.-W., Zelinka, M.D., Terai, C.R., Beydoun, H., Hillman, B.R., Keen, N.D., Caldwell, P.M., and
665 Klein, S.A.: Evaluating Mean State Cloud Properties in the Simple Cloud-Resolving E3SM Atmosphere
666 Model (SCREAM). *J. Adv. Model. Earth Sys.*, 17(11), e2025MS005133, DOI:10.1029/2025MS005133,
667 2025.
- 668 Chin, M., Ginoux, P., Kinne, S., Torres, O., Holben, B.N., Duncan, B.N., Martin, R.V., Logan, J.A.,
669 Higurashi, A., and Nakajima, T.: Tropospheric aerosol optical thickness from the GOCART model and
670 comparisons with satellite and sun photometer measurements. *J. Atmos. Sci.*, 59(3), 461-483, DOI:
671 10.1175/1520-0469(2002)059<0461:TAOTFT>2.0.CO;2, 2002.
- 672 Christensen, M.W., Ma, P.L., Wu, P., Varble, A.C., J. Mülmenstädt, Fast., J.D.: Evaluation of aerosol-
673 cloud interactions in E3SM using a Lagrangian framework. *Atmos. Chem. Phys.*, 23, 2789-2812.
674 DOI:10.5194/acp-23-2789-2023, 2023.
- 675 Darnenov, A., and da Silva A.M.: The Quick Fire Emissions Dataset (QFED) - Documentation of
676 versions 2.1, 2.2 and 2.4, R.D. Koster (Ed.), Technical Report Series on Global Modeling and Data
677 Assimilation, p. 212, NASANASA/TM-2015-104606, 2015.
- 678 Donahue, A.S., Caldwell, P.M., Bertagna, L., Beydoun, H., Bogenschutz, P.A., Bradley, A.M.,
679 Clevenger, T.C., Foucar, J., Golaz, C., Guba, O., Hannah, W., Hillman, B.R., Johnson, J.N., Keen, N., Lin,



- 680 W., Singh, B., Sreepathi, S., Taylor, M.A., Tian, J., Terai, C.R., Ullrich, P.A., Yuan, X., and Zhang, Y.:
681 To exascale and beyond—The Simple Cloud-Resolving E3SM Atmosphere Model (SCREAM), a
682 performance portable global atmosphere model for cloud-resolving scales. *J. Adv. Model. Earth Sys.*, 16,
683 e2024MS004314, DOI:10.1029/2024MS004314, 2024.
- 684 Fast, J.D., Berg, L.K., Alexander, L., Bell, D., D'Ambro, E., Hubbe, J., Kuang, C., Liu, J., Long, C.,
685 Matthews, A., Mei, F., Newsom, R., Pekour, M., Pinterich, T., Schmid, B., Schobesberger, S., Shilling, J.,
686 Smith, J., Springston, S., Suski, K., Thornton, J.A., Tomlinson, J., Wang, J., Xiao, H., and Zelenyuk, A.:
687 Overview of the HI-SCALE field campaign: A new perspective on shallow convective clouds. *Bull.*
688 *Amer. Meteor. Soc.*, 100, 821-420, DOI:10.1175/BAMS-D-18-0030.1, 2019.
- 689 Fast, J.D. Singh, B., Diaz-Ibarra, O., Johnson, J., Dhandapani, C., Gaudet, B., Hassan, T., Huang, M.,
690 Litzinger, J., Overfelt, J., Pressel, K., Schmidt, M., Tang, S., Varble, A.C., Wan, H., Wu, M., Zhang, K.,
691 and Ma, P.-L. 2026. E3SM with the 4-mode Modal Aerosol Module in C++ (MAM4xx).
692 <https://doi.org/10.5281/zenodo.19140449>.
- 693 Forster, P., Storelvmo, T., Armour, K., Collins, W., Dufresne, J. L., Frame, D., et al. The Earth's energy
694 budget, climate feedbacks, and climate sensitivity, (Eds.) In *Climate change 2021: The physical science*
695 *basis. Contribution of working group I to the sixth assessment report of the intergovernmental panel on*
696 *climate change (Chapter 7). Cambridge University Press, 2021.*
- 697 Geiss, A. and Ma, P.-L.: NeuralMie (v1.0): an aerosol optics emulator, *Geosci. Model Dev.*, 18, 1809–
698 1827, DOI:10.5194/gmd-18-1809-2025, 2025.
- 699 Gelaro, R., McCarty, W., Suárez, M.J., Todling, R., Molod, A., Takacs, L., Randles, C., Darmenov, A.,
700 Bosilovich, M.G., Reichle, R., Wargan, K., Coy, L., Cullather, R., Draper, C., Akella, S., Buchard, V.,
701 Conaty, A., da Silva, A., Gu, W., Kim, G.-K., Koster, R., Lucchesi, R., Merkova, D., Nielsen, J.E.,
702 Partyka, G., Pawson, S., Putman, W., Rienecker, M., Schubert, S.D., Sienkiewicz, M., and Zhao, B.: The
703 Modern-Era Retrospective Analysis for Research and Applications, Version 2 (MERRA-2). *J. Climate*,
704 30(13), 5419-5454. DOI:10.1175/JCLI-D-16-0758.1, 2017.
- 705 Golaz, J.-C., VanRoekel, L.P., Zheng, X., Roberts, A.F., Wolfe, J.D., Lin, W., et. al.: The DOE E3SM
706 model version 2: Overview of the physical model and initial model evaluation. *J. Adv. Model. Earth Sys.*,
707 14(12), e2022MS003156. DOI:10.1029/2022MS003156. 2022.
- 708 Kang, L., Marchand, R., Ma, P.-L., Huang, M., Wood, R., Jongeblod, U., and Alexander, B.: Impacts of
709 DMS emissions and chemistry on E3SMv2 simulated cloud droplet numbers and aerosol concentrations
710 over the Southern Ocean. *J. Adv. Model. Earth Sys.*, 17, e2024MS004683. DOI:10.1029/2024MS004683,
711 2025.
- 712 Hassan, T., Zhang, K., Li, J., Singh, B., Zhang, S., Wang, H., and Ma, P.L.: Impacts of spatial
713 heterogeneity of anthropogenic aerosol emissions in a regionally refined global aerosol–climate model.
714 *Geo. Sci. Model Devel.*, 17, 3507-3532, DOI:10.5194/gmd-17-3507-2024, 2024.
- 715 Hersbach, H. Bell, B., Berrisford, P., Hirahara, S., Horányi, A., Muñoz-Sabater, J., Nicolas, J., Peubey, C.,
716 Radu, R., Schepers, D., Simmons, A., Soci, C., Abdalla, S., Abellan, X., Balsamo, G., Bechtold, P.,
717 Biavati, G., Bidlot, J., Bonavita, M., De Chiara, G., Dahlgren, P., Dee, D., Diamantakis, M., Dragani, R.,
718 Flemming, J., Forbes, R., Fuentes, M., Geer, A., Haimberger, L., Healy, S., Hogan, R.J., Hólm, E.,
719 Janisková, M., Keeley, S., Laloyaux, P., Lopez, P., Lupu, C., Radnoti, G., de Rosnay, P., Rozum, I.,
720 Vamborg, F., Villaume, S., and Thépaut, J.-N.; The ERA5global reanalysis. *Quart. J. Roy. Meteor. Soc.*,
721 146, 1999-2049, DOI:10.1002/qj.3803, 2020.
- 722 Huang, M., Ma, P.-L., Varble, A.C., Fast, J.D., Hassan, T., Li, J., Qin, Y., Tang, S., Ullrich, P.A., and
723 Yao, Y.: Evaluation of E3SM simulated aerosols and aerosol-cloud interactions across GCM and
724 convection-permitting scales. *J. Adv. Model. Earth Sys.*, 17(12), e2025MS005288,
725 DOI:10.1029/2025MS005288, 2025.



- 726 Keller, C.A., Knowland, K.E., Duncan, B.N., Liu, J., Anderson, D.C., Das, S., Lucchesi, R.A., Lundgren,
727 E.W., Nicely, J.M., Nielsen, E., Ott, L.E., Saunders, E., Strode, S.A., Wales, P.A., Jacob, D.J., and
728 Pawson, S.: Description of the NASA GEOS Composition Forecast Modeling System GEOS-CF v1.0. *J.*
729 *Adv. Model. Earth Sys.*, 13(4), e2020MS002413, DOI:10.1029/2020MS002413, 2021.
- 730 Khain, A., Lynn, B., and Gavze, E.: Effect of mutual cloud–aerosol interaction on a mesoscale convective
731 system. *J. Atmos. Sci.*, 82(12), 2693–2710, DOI:10.1175/JAS-D-25-0056.1, 2025.
- 732 Larson, V.E., Golaz, J.-C., and Cotton, W.R.: Small-scale and mesoscale variability in cloudy boundary
733 layers: Joint probability density functions. *J. Atmos. Sci.*, 59(24), 3519–3539, DOI:10.1175/1520-
734 0469(2002)059<3519:SSAMVI>2.0.CO;2, 2002.
- 735 Liu, X., Easter, R.C., Ghan, S.J., Zaveri, R., Rasch, P., Shi, X., Lamarque, J.-F., Gettelman, A., Morrison,
736 H., Vitt, F., Conley, A., Park, S., Neale, R., Hannay, C., Ekman, A.M.L., Hess, P., Mahowald, N.,
737 Collins, W., Iacono, M.J., Bretherton, C.S., Flanner, M.G., and Mitchell, D.: Toward a minimal
738 representation of aerosols in climate models: description and evaluation in the Community Atmosphere
739 Model CAM5. *Geosci. Model Dev.*, 5, 709–739, DOI:10.5194/gmd-5-709-2012, 2012.
- 740 Liu, X., Ma, P.-L., Wang, H., Tilmes, S., Singh, B., Easter, R. C., Ghan, S. J., and Rasch, P. J.:
741 Description and evaluation of a new four-mode version of the Modal Aerosol Module (MAM4) within
742 version 5.3 of the Community Atmosphere Model. *Geosci. Model Dev.*, 9, 505–522, DOI:10.5194/gmd-9-
743 505-2016, 2016.
- 744 Lu, Z., Liu, X., Ke, Z., Zhang, K., Ma, P.-L., & Fan, J.: Incorporating an interactive fire plume-rise model
745 in the DOE's energy exascale earth system model version 1 (E3SMv1) and examining aerosol radiative
746 effect. *J. Adv. Model. Earth Sys.*, 16, e2023MS003818, DOI:10.1029/2023MS003818, 2024.
- 747 Ma, P.L., Rasch, P.J., Fast, J.D., Easter, R.C., Gustafson Jr., W.I., Liu, X., Ghan, S.J., and Singh, B.:
748 Assessing the CAM5 physics suite in the WRF-Chem model: Implementation, evaluation, and resolution
749 sensitivity. *Geosci. Model Dev.*, 7, 755–778. DOI:10.5194/gmd-7-755-2014, 2014.
- 750 Mahfouz, N.G., Beydoun, H., Mülmenstädt, J.H., Keen, N.D., Varble, A.C., Bertagna, L., Bogenschutz,
751 P., Bradley, A., Christensen, M., Clevenger, T.C., Donahue, A., Fast, J., Foucar, J., Golaz, J.-C., Guba,
752 O., Hannah, W., Hillman, B., Jacob, R., Lin, W., Ma, P.-L., Qian, Y., Singh, B., Terai, C., Wang, H., Wu,
753 M., Zhang, K., Gettelman, A., Taylor, M., Leung, L.R., Caldwell, P., and Burrows, S.: Prescribing the
754 aerosol effective radiative forcing in the Simple Cloud-Resolving E3SM Atmosphere Model v1. *Atmos.*
755 *Chem. Phys.* 25, 15105–15120. DOI:10.5194/acp-25-15105-2025, 2025.
- 756 McCoy, D.T., Field, P., Gordon, H., Elsaesser, G.S., and Grosvenor, D.P.: Untangling causality in
757 midlatitude aerosol–cloud adjustments. *Atmos. Chem. Phys.*, 20, 4085–4103. DOI:10.5194/acp-20-4085-
758 2020, 2020.
- 759 Mills, M.J., Richter, J.H., Tilmes, S., Kravitz, B., MacMartin, D.G., Glanville, A.A., Tribbia, J.J.,
760 Lamarque, J.-F., Vitt, F., Schmidt, A., Gettelman, A., Hannay, C., Bacmeister, J.T., and Kinnison, D.E.:
761 Radiative and chemical response to interactive stratospheric sulfate aerosols in fully coupled
762 CESM1(WACCM). *J. Geophys. Res.-Atmos.*, 122, 13061–13078, DOI:10.1002/2017JD027006, 2017.
- 763 Morrison, H., and Gettelman, A.: A new two-moment bulk stratiform cloud microphysics scheme in the
764 Community Atmosphere Model, version 3 (CAM3). Part I: Description and numerical tests. *J. of Climate*,
765 21(15), 3642–3659, DOI:10.1175/2008JCLI2105.1, 2008.
- 766 Morrison, H., and Milbrandt, J.A.: Parameterization of cloud microphysics based on the prediction of
767 bulk ice particle properties. Part I: Scheme description and idealized tests. *J. Atmos. Sci.*, 72(1), 287–311,
768 DOI:10.1175/JAS-D-14-0065.1, 2015.
- 769 Parworth, C., Fast, J.D., Mei, F., Shippert, T., Sivaraman, C., Tilp, A., Watson, T., and Zhang, Q.: Long-
770 term measurements of submicrometer aerosol chemistry at the ARM Southern Great Plains (SGP) site



- 771 using an Aerosol Chemical Speciation Monitor (ACSM). *Atmos. Environ.*, 106, 45-55,
772 DOI:10.1016/j.atmosenv.2015.01.060, 2015.
- 773 Petters, M.W., and Kreidenweis, S.M.: A single parameter representation of hygroscopic growth and
774 cloud condensation nucleus activity. *Atmos. Chem. Phys.* 7, 1961-1971, DOI:10.5194/acp-7-1961-2007,
775 2007.
- 776 Pincus, R., Mlawer, E.J. and Delamere, J.S. Balancing accuracy, efficiency, and flexibility in radiation
777 calculations for dynamical models. *J. Adv. Model. Earth Sys.*, 11(10), 3074–3089,
778 DOI:10.1029/2019MS001621, 2019.
- 779 Randles, C.A., da Silva, A.M., Buchard, V., Colarco, P.R., Darmenov, A., Govindaraju, R., Smirnov, A.,
780 Holben, B., Ferrare, R., Hair, J., Shinozuka, Y., and Flynn, C.J.: The MERRA-2 aerosol reanalysis, 1980
781 onward, Part I: System description and data assimilation evaluation. *J. Climate*, 30, 6823–6850,
782 DOI:10.1175/JCLI-D-16-0609.1, 2017.
- 783 Shan, Y., Fan, J., Zhang, K., Shpund, J., Terai, C., Zhang, G.J., Song, X., Chen, C.C.J., Lin, W. Liu, X.,
784 Shrivastava, M., Wang, H., and Xie, S.: Improving aerosol radiative forcing and climate in E3SM:
785 Impacts of new cloud microphysics and improved wet removal treatments. *J. Adv. Model. Earth Sys.*, 16,
786 e2023MS004059, DOI:10.1029/2023MS004059, 2024.
- 787 Shi, Y., Liu, X., Wu, C., Lu, Z., Zhang, K., and Ma, P.-L.: Representing anthropogenic dust from
788 agricultural sources in E3SMv1: Implementation, evaluation, and assessment of the radiative forcing. *J.*
789 *Adv. Model. Earth Sys.*, 17, e2023MS003925. DOI:/10.1029/2023MS003925, 2025.
- 790 Silva, S. J., Ma, P.-L., Hardin, J. C., and Rothenberg, D.: Physically regularized machine learning
791 emulators of aerosol activation. *Geosci. Model Dev.*, 14, 3067–3077, DOI:10.5194/gmd-14-3067-2021,
792 2021.
- 793 Stanford, M., Varble, A.C., Feng, Z., Fast, J., Gustafson Jr., W.I., Glienke, S., and Zhang, Z.: Warm-
794 phase microphysical contributions to the “popcorn” convection precipitation simulation bias. Submitted
795 to *J. Geophys. Res.* 2026.
- 796 Stevens, B., Satoh, M., Auger, L., Biercamp, J., Bretherton, C.S., Chen, X., Düben, P., Judt, F.,
797 Khairoutdinov, M., Klocke, D., Kodama, C., Kornbluh, L., Lin, S.-J., Neumann, P., Putman, W.M.,
798 Röber, N., Shibuya, R., Vanniere, B., Vidale, P.L., Wedi, N., and Zhou, L.: DYAMOND: the DYnamics
799 of the Atmospheric general circulation Modeled On Non-hydrostatic Domains, *Prog. Earth Planet. Sci.*,
800 6, 61, DOI:10.1186/s40645-019-0304-z, 2019.
- 801 Stokes, G.M., and Schwartz, S.E.: The Atmospheric Radiation Measurement (ARM) program:
802 Programmatic background and design of the cloud and radiation testbed. *Bull. Amer. Meteor. Soc.*, 75(7),
803 1201–1221, DOI:10.1175/1520-0477(1994)075<1201:TARMPP>2.0.CO;2, 1994.
- 804 Su, T., Zhang, Y., Ma, H.-Y., Varble, A.C., and Bogenschutz, P.A.: Diagnosing convective biases in the
805 DOE global storm-resolving model: Insights from regionally refined simulations during the CACTI
806 campaign. *J. Geophys. Res. Atmos.*, In Press. 2026.
- 807 Twomey, S.: Pollution and the planetary albedo. *Atmos. Environ.*, 8, 1251-1256, 1974.
- 808 Tang, S., Fast, J.D., Zhang, K., Shilling, J.E., Mei, F., Zawadowicz, M.A., Varble, A.C., and Ma, P.L.:
809 Earth System Model Aerosol-Cloud Diagnostics package (ESMAC Diags) version 1: Assessing E3SM
810 aerosol predictions using aircraft, ship, and surface measurements. *Geo. Model Devel.*, 15, 4055–4076,
811 DOI:10.5194/gmd-15-4055-2022, 2022.
- 812 Tang, S., Varble, A.C., Fast, J.D., Zhang, K., Wu, P., Dong, X., Mei, F., Pekour, M., Hardin, J.C., and
813 Ma, P.L.: Earth System Model Aerosol-Cloud Diagnostics package (ESMAC Diags) Version 2:
814 Assessments of aerosols, clouds and aerosol-cloud interactions through field campaign and long-term
815 observations. *Geo. Model Dev.*, 16, 6355-6376, DOI:10.5194/gmd-2023-51, 2023.



- 816 Taylor, M., Caldwell, P.M., Bertagna, L., Clevenger, C., Donahue, A., Foucar, J., et. al.: The Simple
817 Cloud-Resolving E3SM Atmosphere Model running on the Frontier exascale system. In *Proceedings of*
818 *the International Conference for High Performance Computing, Networking, Storage and Analysis.*
819 Association for Computing Machinery. DOI:10.1145/3581784.3627044, 2023.
- 820 Terai, C.R., Pritchard, M.S., Blossey, P., and Bretherson, C.S.: The impact of resolving subkilometer
821 processes on aerosol-cloud interactions of low-level clouds in global model simulations. *J. Adv. Model.*
822 *Earth Sys.*, 20, e2020MS002274, DOI:10.1029/2020MS002274. 2020.
- 823 Terai, C.R., Keen, N.D., Caldwell, P.M., Beydoun, H., Bogenschütz, P.A., Chao, L.-W., Hillman, B.R.,
824 Ma, H.-Y., Zelika, M.D., Bertagna, L., Bradley, A.M., Clevenger, T.C., Donahue, A.S., Foucar, J., Golaz,
825 J.-C., Guba, O., Hannah, W., Lee, J., Lin W., Mahfouz, N., Mülmenstädt J., Salinger, A.G., Singh, B.,
826 Sreepathi, S., Qin, Y., Taylor, M.A., Ullrich, P.A., Wu, W.-Y., Yuan, X., Zender, C.S., and Zhang, Y.;
827 Radiative, hydrologic, and circulation responses to warming in Cess-Potter simulations using the global
828 3.25-km SCREAM. *J. Adv. Model. Earth Sys.*, 17, e2024MS004930. DOI:10.1029/2024MS004930.
- 829 Tian, J., Zhang, Y., Klein, S.A., Terai, C.R., Caldwell, P.M., Beydoun, H., Bogenschütz, P., Ma, H.-Y.,
830 and Donahue, A.S.: How well does the DOE global storm resolving model simulate clouds and
831 precipitation over the Amazon? *Geophys. Res. Lett.*, 51(14), e2023GL108113,
832 DOI:10.1029/2023GL108113, 2024.
- 833 Tilmes, S., Mills, M.J., Zhu, Y., Bardeen, C.G., Vitt, F., Yu, P., Fillmore, D., Liu, X., Toon, B., and
834 Deshler, T.: Description and performance of a sectional aerosol microphysical model in the Community
835 Earth System Model (CESM2). *Geo. Sci. Model Devel.*, 16, 6087-6125, DOI:10.5194/gmd-16-6087-
836 2023, 2023.
- 837 Trott, C.R., Lebrun-Grandié, D., Arndt, D., Ciesko, J., Dang, V., Ellingwood, N., et al.: Kokkos3:
838 Programming model extensions for the exascale era. *IEEE Transactions on Parallel and Distributed*
839 *Systems*, 33(4), 805–817. DOI:10.1109/TPDS.2021.3097283, 2022.
- 840 Varble, A.C., Ma, P.-L., Christensen, M.W., Mülmenstädt, J., Tang, S., and Fast, J.: Evaluation of liquid
841 cloud albedo susceptibility in E3SM using coupled eastern North Atlantic surface and satellite retrievals.
842 *Atmos. Chem. Phys.*, 23, 13523-13553, DOI:10.5194/acp-23-13523-2023, 2023.
- 843 Van der Werf, G., Randerson, J.T., Giglio, L., Van Leeuwen, T.T., Chen, Y., Rogers, B.M., Mu, M., Van
844 Marle, M.J.E., Morton, D.C., Collatz, G.J., Yokelson, R.J., and Kasibhatla, P.S.: Global fire emissions
845 estimates during 1997–2016. *Earth Sys. Sci. Data.*, 9, 697-720, DOI: 0.5194/essd-9-697-2017, 2017.
- 846 Wu, M., Wang, H., Easter, R.C., Lu, Z., Liu, X., Singh, B., Ma, P.L., Tang, Q., Zaveri, R.A., Ke, Z.,
847 Zhang, R., Emmons, L.K., Tilmes, S., Dibb, J.E., Zheng, X., Xie, S., and Ruby Leung, L.R.:
848 Development and evaluation of E3SM-MOSAIC: Spatial distributions and radiative effects of nitrate
849 aerosol. *J. Adv. Model. Earth Sys.*, 14, e2022MS00357, DOI:10.1029/2022MS003157, 2022.
- 850 Wang, H., Easter, R.C., Zhang, R., Ma, P.L., Singh, B., Zhang, K., Ganguly, D., Rasch, P.J., Burrows,
851 S.M., Ghan, S.J., Lou, S., Qian, Y., Yang, Y., Feng, Y., Flanner, M., Leung, L.R., Liu, X., Shrivastava,
852 M., Sun, J., Tang, Q., Xie, S., Yoo, J.-H.: Aerosols in the E3SM Version 1: New developments and their
853 impacts on radiative forcing. *J. Adv. Model. Earth Sys.*, 12, e2019MS001851,
854 DOI:10.1029/2019MS001851, 2020.
- 855 Wang, W., Liu, X., Lin, G., Lu, Z., and Wu, C.: The Impact of model horizontal resolution on aerosol
856 modeling over East Asia using variable-resolution CESM2. *J. Geophys. Res.*, 130(12), e2025JD043518,
857 DOI:10.1029/2025JD043518, 2025.
- 858 Wang, Y., Ma, P.L., Peng, J., Zhang, R., Jiang, J.H., Easter, R.C., and Yung, Y.L.: Constraining aging
859 processes of black carbon in the Community Atmosphere Model using environmental chamber
860 measurements. *J. Adv. Model. Earth Sys.*, 10, 2514-2526, DOI:10.1029/2018MS001387, 2018.



- 861 Wang, H, Wu, M., Ke, Z., Feng, Y., Shrivastava, M., Tang, Q., Wan, H., Liu, X., Easter, R.C., Lin, W.,
862 Singh, B., Terai, C.R., Burrows, S.M., Fan, J., Ma, P.-L., Mahfouz, N., Mülmenstädt, J., Qian, Y., Shan,
863 Y., Zhang, K., Zhang, Y., Leung, L.R., Xie, S., and Rasch, P.J.: Overview of aerosols in the E3SM
864 Version 3: New model features and their impacts. 2026.
- 865 Zhang, Z., Varble, A.C., Feng, Z., Marquis, J., Hardin, J., and Zipser, E.: Dependencies of simulated
866 convective cell and system growth biases on atmospheric instability and model resolution. *J. Geophys.*
867 *Res. Atmos.*, 129(22), e2024JD041090, DOI:10.1029/2024JD041090, 2024.
- 868 Zhao, B., Donahue, N.M., Zhang, K., Mao, L., Shrivastava, M., Ma, P.L., Shen, J., Wang, S., Sun, J.,
869 Gordon, H., Tang, S., Fast, J.D., Wang, M., Gao, Y., Yan, C., Singh, B., Li, Z., Huang, L., Lou, S., Lin,
870 G., Wang, H., Jiang, J., Ding, A., Nie, W., Qi, X., Chi, X., and Wang, L. Global variability in atmospheric
871 new particle formation mechanisms. *Nature*, 631, 98-105, DOI:10.1038/s41586-024-07547-1, 2024.
- 872
- 873



874 Table 1. Aerosol species in MAM4xx and GEOS-FP

MAM4		GEOS-FP	
Aerosol Specie Name	Description	Aerosol Specie Name	Description
bc_a1	accumulation mode black carbon	bcphilic	hydrophilic black carbon
bc_a3	coarse mode black carbon	bcphobic	hydrophobic black carbon
bc_a4	carbon mode black carbon	ocphilic	hydrophilic organic carbon
pom_a1	accumulation mode primary organic matter	ocphobic	hydrophobic organic carbon
pom_a3	coarse mode primary organic matter	so4	sulfate
pom_a4	carbon mode primary organic matter	du001	dust bin 1
soa_a1	accumulation mode SOA	du002	dust bin 2
soa_a2	Aitken mode SOA	du003	dust bin 3
soa_a3	coarse mode SOA	du004	dust bin 4
mom_a1	accumulation mode marine organic matter	du005	dust bin 5
mom_a2	Aitken mode marine organic matter	ss001	sea-salt bin 1
mom_a3	coarse mode marine organic mater	ss002	sea-salt bin 2
mom_a4	carbon mode marine organic matter	ss003	sea-salt bin 3
so4_a1	accumulation mode sulfate	ss004	sea-salt bin 4
so4_a2	Aitken mode sulfate	ss005	sea-salt bin 5
so4_a3	coarse mode sulfate		
dst_a1	accumulation mode dust		
dst_a3	coarse mode dust		
nacl_a1	accumulation mode sea salt		
nacl_a2	Aitken mode sea salt		
nacl_a3	coarse mode sea salt		



num_a1	accumulation mode aerosol number		
num_a2	Aitken mode aerosol number		
num_a3	coarse mode aerosol number		
num_a4	primary carbon mode aerosol number		

875